

Geometrically Designing the Kinematic Behavior of Catalytic Nanomotors

J. G. Gibbs,^{*,†} S. Kothari,[‡] D. Saintillan,[‡] and Y.-P. Zhao[†]

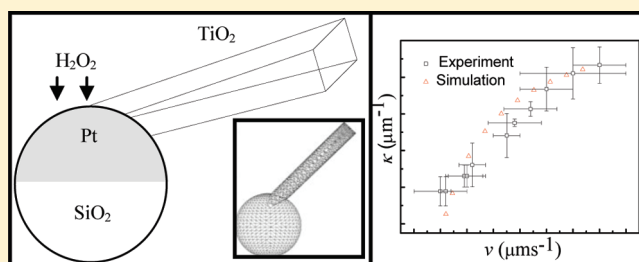
[†]Nanoscale Science and Engineering Center, Department of Physics and Astronomy, The University of Georgia, Athens, Georgia 30602, United States

[‡]Department of Mechanical Science and Engineering, University of Illinois at Urbana–Champaign, Urbana, Illinois 61801, United States

S Supporting Information

ABSTRACT: Catalytic nanomotors with silica microbead heads and TiO₂ arms are systematically designed by dynamic shadowing growth. The swimming trajectories are fine tuned by altering the arm length and orientation exploiting geometry-dependent hydrodynamic interactions at low Reynolds number. The curvature, angular frequency, and radius of curvature of the trajectories change as a function of arm length. Simulations based on the method of regularized Stokeslets are also described and correctly capture the trends observed in the experiments.

KEYWORDS: Nanomotors, oblique angle deposition, glancing angle deposition, regularized Stokeslet



Catalytic nanomotors are nano-to-microsized actuators converting chemical energy into kinetic energy through a catalyzed reaction using an on-board catalyst. Nature¹ provides researchers with models by which to design inorganic artificial nanomotors, and several avenues have been traversed to mimic naturally occurring biomotors.^{2–7} A wide range of data coupled with theory are found in the literature focusing upon the design,^{8–17} motion analysis,^{18–23} assembly,^{3,8,9,24–26} physical and chemical mechanisms,^{4,10,11,16,18,21,27,28} and the control or modulation of motion of micrometer and nanometer scale motors. The latter is becoming the focus with the use of manipulation by fields^{15,29–31} (including light²⁴), thermal modulation,³² varying catalytic alloys,²² and geometric design.^{10,13–17,19} Many systems studied to date have not focused upon the geometry of nanomotors or how altering the shapes and dimensions influence movement. Exceptions include the gear-shaped spinning structure,¹⁰ L-shaped and spiral catalytic nanomotors,¹⁴ and magnetic propellers.¹⁵ The shape of microswimmers does however greatly affect the types of swimming behaviors observed. This fact is especially important for autonomous machines since no external manipulation is present, and control is difficult to achieve.

Much of the catalytic nanomotor research to date implements template-directed electroplating (TDEP) for fabrication; examples include striped Au/Pt nanowires^{4,10,11,13,18–20,27,29} and, combining with lithography, Au/Pt gears.¹⁰ Since the structural morphology is dependent upon the template shape with TDEP, the method is not the most effective for controlling the geometry since it is limited to the shape of the template; a common example is the use of anodized alumina membranes, which produce cylindrical nanowires. Bimetallic nanowire nanomotors move translationally in the direction of the catalyst, an effect of self-electrophoresis,²⁷ unless controlled by external fields,²⁹ or

rotational motion can be observed when one end is tethered to the surface.⁴ Besides TDEP, other fabrication techniques include heterosectioned nanomotors fabricated by tethering the catalyst to the particle¹² and the evaporation of a catalyst onto the particle using physical vapor deposition (PVD).^{16,21,23}

A PVD fabrication method known as dynamic shadowing growth (DSG) is more versatile for systematically designing catalytic nanomotors. DSG is a PVD coating method that combines substrate manipulation with the shadowing effect allowing for the fabrication of an array of nanostructures; the programming of the substrate movement determines the type of nanostructure that results from the deposition. DSG allows for a wider range of shapes than TDEP due to this programmability. Some examples developed in our lab include L-shaped and spiral nanomotors¹⁴ as well as multicomponent rotary structures.¹⁷ The Pt catalyst is easily deposited in a manner that best suits the type of motion desired. Also, catalytic nanomotors are easily and cheaply fabricated with this method, and a large yield of uniform structures may be obtained.^{14,17} DSG is effective for controlling particle geometry; therefore, it is an appropriate method to perform a detailed study on the effects of geometry on the swimming characteristics. Here we devote our study to fine-tuning geometries of similarly shaped structures to gain a broader understanding of the importance of morphology in nanomotor engineering. By utilizing DSG to break the symmetry of a spherical microbead by adding an oxide nanoarm of different lengths and orientations, the relationship between the motion behaviors observed and the length and orientation of the arm can be studied. The trajectories also change as a function of the speed of the structures when varying the concentration of the

Received: April 15, 2011

Published: May 20, 2011

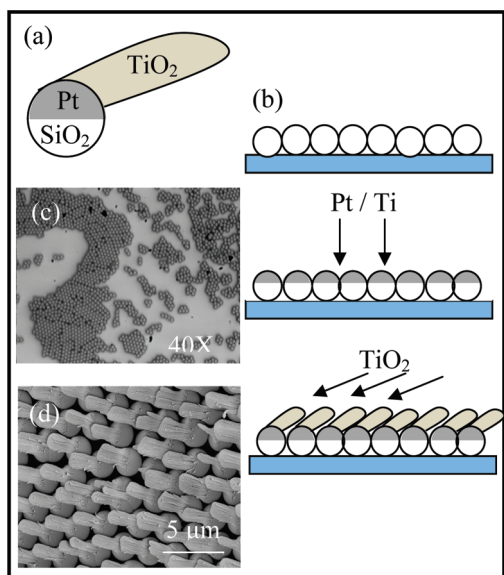


Figure 1. (a) Schematic of the Pt-coated microbead with a TiO₂ arm; (b) schematic of monolayer of silica microbeads, Ti and Pt, are evaporated onto the monolayer, and schematic of the deposition of the TiO₂ arms at a large angle; (c) optical micrograph of the monolayer under 40× magnification; (d) SEM top-view of the monolayer with TiO₂ arms.

propelling fuel H₂O₂. Numerical calculations based on a detailed solution of the equations of low-Reynolds-number flow are also performed, and the numerical and experimental results agree.

An asymmetrical nanomotor consisting of a spherical microbead with an arm extending to different lengths and angles was fabricated to alter the swimming behavior as shown in Figure 1a. A self-assembled monolayer of silica microbeads of 2.01 μm in diameter (Bangs Laboratories) is dispersed on a clean 2 cm × 2 cm Si substrate by diluting the microbeads in methanol (1:5 ratio) and dropping 3 μL by pipet onto the Si wafer surface. A cross-section depiction of the fabrication process is shown in Figure 1b. A 40× optical micrograph of the resultant monolayer is shown in Figure 1c; many of the microbeads are arranged in a close-packed monolayer. A 10 nm thin film of Ti is first evaporated onto the beads by electron beam evaporation as an adhesion layer followed by a 50 nm Pt deposition. For these two thin-film depositions, the vapor incidence direction is parallel to the substrate surface normal. The substrate is then tilted to an angle of 86° with respect to the vapor incidence direction, and a thick layer of TiO₂ is evaporated onto the monolayer to grow the arm. This large-angle deposition method is known as oblique angle deposition (OAD), which is a subclass of DSG. An example of the result may be seen in a top-view SEM micrograph shown in Figure 1d. During the deposition, the thickness of the deposited films is monitored in situ by a quartz crystal microbalance (QCM) that directly faces the vapor. The TiO₂ was evaporated to 5 different QCM-reading lengths: 1.25 μm, 2.5 μm, 3.75 μm, 5 μm, and 6.25 μm. Another structure was fabricated using glancing angle deposition (GLAD), which combines OAD and substrate rotation. GLAD is accomplished by rotating the substrate azimuthally at a constant speed during OAD deposition of the TiO₂. Because the substrate rotates continually, the microbeads receive vapor from all azimuthal directions often resulting in an arm that is perpendicular to the substrate surface. For the GLAD

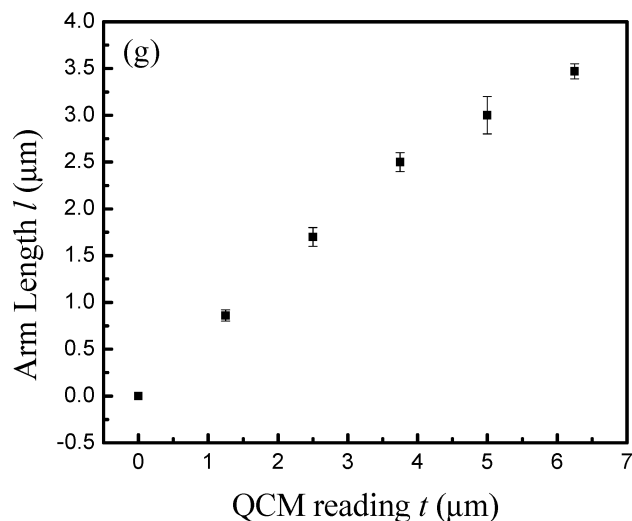
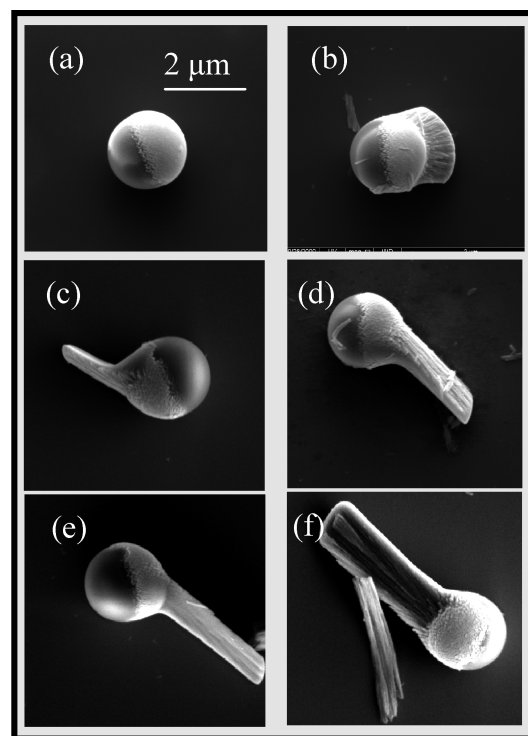


Figure 2. SEM of the structures removed from the substrate with arms of various lengths l = (a) 0 μm; (b) 0.86 μm; (c) 1.7 μm; (d) 2.5 μm; (e) 3.0 μm; (f) 3.5 μm; and (g) oxide arm length versus QCM reading.

TiO₂ structure, the QCM reading reached 7 μm while the substrate rotation speed remained at ~22.5°/sec.

SEM images were taken of each sample in order to analyze the morphology of the structures, and these images were obtained by dropping nanomotor suspensions onto clean Si wafers and allowing the droplets to dry. As the droplets dry, the orientation of the nanomotors as they adhere to the wafers is random; this allows us to closely observe the structures' morphologies by looking at a large number of structures oriented in different directions. Figure 1a shows the nanomotor structure that is comprised of a spherical microbead half-coated with Pt and a TiO₂ arm extending from the top of the Pt section. Since the Pt is evaporated at 0°, the microbead has two hemispheres: one silica and one Pt. As a result of the deposition process in which the TiO₂ is

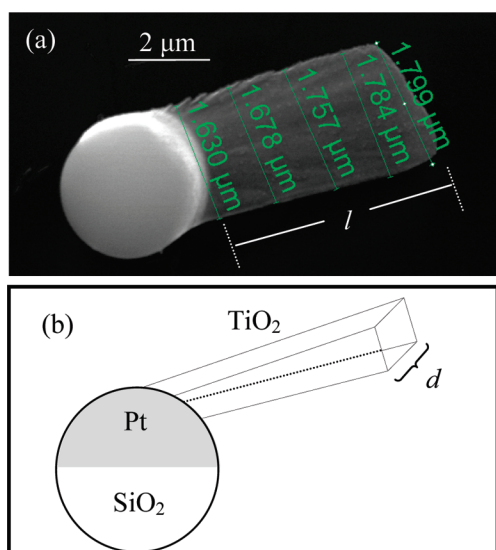


Figure 3. (a) SEM of an OAD-grown nanomotor with the TiO₂ arm increasing in width, d , as the length, l , increases; (b) side-view schematic showing the width, d , of the oxide arm.

deposited at a large angle described in the fabrication section, the arm is tilted at an angle with respect to the line defining the separation of the two hemispheres between the Pt coating and the bare silica as seen in Figure 1a. The original monolayer onto which we evaporate Pt and TiO₂ is not a complete monolayer; there are domains on the substrate that do not have any microbeads present as can be seen in Figure 1c. Since the monolayer is not complete, not all of the structures are the same after the deposition. Because of the shadowing effect, the microbeads that are completely surrounded in the closely packed crystal have a different morphology than the microbeads on the edge of the domain. The former make up the vast majority of the structures, and the structures that result from shadowing on the edge of the domain are relatively rare so we do not consider these for the analysis. For the nanomotors resulting from within the domain, the arms grow from the top of microbeads only due to the shadowing of the adjacent microbeads forming fan bladelike arms. The SEM image in Figure 1d shows the final structure still in a closely packed monolayer.

Figure 2 shows representative SEM images of individual nanomotors of various arm lengths. Figure 2a shows a Pt-coated sphere with no TiO₂; Figure 2b has a short TiO₂ arm, and in this image, the arm is facing downward toward the Si wafer; Figure 2c–e shows side-views of the nanomotors and the TiO₂ arms are flat; Figure 2f shows the longest structure that is oriented in such a manner as to show the side and top of the structure simultaneously. The structures shown in Figure 2 are examples of each nanomotor studied with QCM thickness reading $t = 1.25, 2.5, 3.75, 5,$ and $6.25 \mu\text{m}$ shown in Figures 2a–f, respectively. For OAD, the actual length of the oxide arm does not correspond to the QCM reading since the substrate has an angle of 86° with respect to the vapor incidence direction while the QCM itself is faced directly toward the vapor; because of the large angle, a smaller amount of material accumulates on the substrate than on the QCM. The graph in Figure 2g shows actual measured arm lengths, l , defined in Figure 4a versus the QCM reading thickness, t . The actual length l is significantly shorter than the QCM reading, t ; the actual lengths measured using SEM are as follows: $t = 1.25 \mu\text{m}, l = 0.86 \pm 0.06 \mu\text{m}$;

$t = 2.5 \mu\text{m}, l = 1.7 \pm 0.1 \mu\text{m}$; $t = 3.75 \mu\text{m}, l = 2.5 \pm 0.1 \mu\text{m}$; $t = 5 \mu\text{m}, l = 3.0 \pm 0.2 \mu\text{m}$; and $t = 6.25 \mu\text{m}, l = 3.47 \pm 0.08 \mu\text{m}$. As the oxide layer accumulates, the width of the TiO₂ arm tends to increase as the length of the arm increases as shown in Figure 3a. The width of the arm is slightly smaller than the diameter of the microbead at the base of the arm, and the arm tends to “fan out” at the ends. As an example, in Figure 3a the width of the arm increases from $d = 1.6$ – $1.8 \mu\text{m}$. Figure 3b illustrates the fanning phenomenon and defines the value of the width of the arm, d . The fan shape can also be seen in Figure 2b,e as well. Side-view images show that the arms are rather thin as can be seen in Figure 2c,d, so the structures do quite resemble fan blades.

Nanomotor dimensions fall in the range of a few hundred nanometers to several micrometers, placing them in the low-Reynolds-number flow regime in which nanomotor motion is dominated by viscous drag forces. The dimensionless Reynolds number, or ratio between inertial forces and viscous forces, is defined as $\text{Re} = \rho v L / \mu$, where ρ is the fluid density, μ is the fluid dynamic viscosity, v is a characteristic velocity (for instance the translational velocity of the nanomotor), and L is the characteristic dimension of the particle.^{33,34} For example, a nanomotor of dimension $L = 5 \mu\text{m}$ moving at $v = 10 \mu\text{m s}^{-1}$ in water, $\text{Re} = 5 \times 10^{-5} \ll 1$. When $\text{Re} \ll 1$, inertial terms in the Navier–Stokes equations may be ignored, reducing them to the linearized time-independent Stokes equations $\nabla p = \mu \nabla^2 \mathbf{v}$, $\nabla \cdot \mathbf{v} = 0$ where p is the pressure, and \mathbf{v} is the fluid velocity. For a catalytic nanomotor, viscous drag dominates, which implies that the nanomotor motion is governed by its shape. As an example, the famous Stokes’ drag law for a spherical particle translating at low Reynolds number is given by $\mathbf{F}_s^D = -6\pi\mu a \mathbf{v}$, where a is the radius of the sphere; the sphere is symmetrical and isotropic, so no torque is induced. For a catalytically driven spherical nanomotor, if sufficient fuel exists in the solution, the catalyzed reaction propels the particle, which, in the absence of inertia, quickly reaches a steady-state motion, in which the driving force, \mathbf{F} , and the drag force, \mathbf{F}_s^D , are equal in magnitude but antiparallel. \mathbf{F} , the resultant force from the catalytic reaction, depends upon the reaction rate and the surface area of the catalyst. Because of symmetry, a swimming nano- or microsphere of electrically insulating material moves translationally in the direction away from the catalyst site.²¹ If the symmetry of the sphere is broken by adding the oxide arm as shown in Figure 1a, the hydrodynamic drag will now cause the particle to rotate in addition to moving translationally. The drag force on the arm, \mathbf{F}_a^D , is off-centered from the driving force, leading to a net hydrodynamic torque on the structure, which couples translational and rotational motions.

To fully capture the motion of the nanomotors and elucidate the coupling between translation and rotation, the equations of microhydrodynamics have to be considered.³⁴ In linear Stokes flow, the hydrodynamic force and torque on a rigid particle depend linearly on the particle motion via the following resistance formulation³³

$$\begin{bmatrix} \mathbf{F} \\ \mathbf{T} \end{bmatrix} = \begin{bmatrix} \mathbf{A} & \mathbf{B}^T \\ \mathbf{B} & \mathbf{C} \end{bmatrix} \begin{bmatrix} \mathbf{v} \\ \boldsymbol{\omega} \end{bmatrix} \quad (1)$$

where \mathbf{F} is the hydrodynamic force, \mathbf{T} is the hydrodynamic torque, \mathbf{v} is the translational velocity, $\boldsymbol{\omega}$ is the angular velocity, and \mathbf{A} , \mathbf{B} , and \mathbf{C} are second-order tensors dependent upon the geometry.³⁴ The 6×6 matrix appearing on the right-hand side of eq 1 is known as the resistance matrix. To calculate this matrix, a solution of the Stokes equations in the geometry of interest is

required. While such a solution can be obtained analytically for particles with simple shapes (spheres, spheroids, etc.) in unbounded domains, numerical solutions are required for complex shapes or particles in the vicinity of boundaries, such as the asymmetric nanomotors considered in this study, which evolve next to a rigid substrate.

Here, we describe simulations that include an accurate representation of the nanomotor geometry, full hydrodynamic interactions between components of the nanomotor and with the supporting substrate, Brownian motion as a result of thermal fluctuations, as well as frictional forces with the substrate. A typical geometry is illustrated in Figure 4 and is composed of a rigid sphere connected to a section of an ellipsoid to model the fanlike shape of the arm in the experiments. By removing sections of different lengths on the free end of the ellipsoid, various arm lengths can be modeled for direct comparison with the experimental results. Particle dynamics are captured using the method of regularized Stokeslets,³⁵ which is a variant of the classic boundary integral method for linearized viscous flow,³⁶ and allows for the direct numerical calculation of the resistance matrix of eq 1. Hydrodynamic interactions with the walls are accounted for using the method of images for regularized Stokeslets,^{37,38} which makes use of a regularized version of the classic Green's function for Stokes flow in the vicinity of a no-slip wall.³⁹ The method was tested extensively for simple particle shapes (spheres, spheroids) and showed very good agreement with previously published results down to short separation distances.³³ Once the resistance matrix is obtained, its inverse, known as the mobility matrix, can be calculated and used to determine particle velocities resulting from a prescribed catalytic force, from which trajectories are inferred using a time-marching algorithm. To qualitatively reproduce the trends seen in experiments, we find that including a frictional force and torque with the substrate (in addition to the driving force due to the catalytic reaction) is required. Several models for friction were investigated, and best agreement with the experimental data was obtained using the model of Liu and Bhushan^{40,41} for velocity-dependent friction at the micro- and nanoscales, which expresses the frictional force and torque on the particle in terms of its linear and angular velocities using an affine relationship. Because the velocities themselves depend linearly on the catalytic propulsion force f , the frictional force and torque may be expressed as

$$F = F_0 + (F_1 - F_0) \frac{f - f_0}{f_1 - f_0} \quad (2)$$

$$T = T_0 + (T_1 - T_0) \frac{f - f_0}{f_1 - f_0} \quad (3)$$

where $f_1 = 1.2$ pN and $f_0 = 0.4$ pN are estimates for the minimum and maximum values of the catalytic propulsive force in the experiments, and the four unknown parameters F_0 , T_0 and F_1 , T_1 correspond to the maximum and minimum attainable values of the frictional force and torque, respectively. The values of these four constants were adjusted to match experimental data for the trajectory curvatures, and in our simulations, the following values are used: $F_0 = 0.001$ pN, $F_1 = 0.0018$ pN, $T_0 = 0.0000107$ fN·m, $T_1 = 0.000025$ fN·m. Finally, Brownian fluctuations are included using the Langevin equation in which the magnitude of the random displacements is calculated from the mobility matrix to satisfy the fluctuation–dissipation theorem of statistical mechanics.⁴² A more detailed description of the numerical methods is deferred to a future publication.

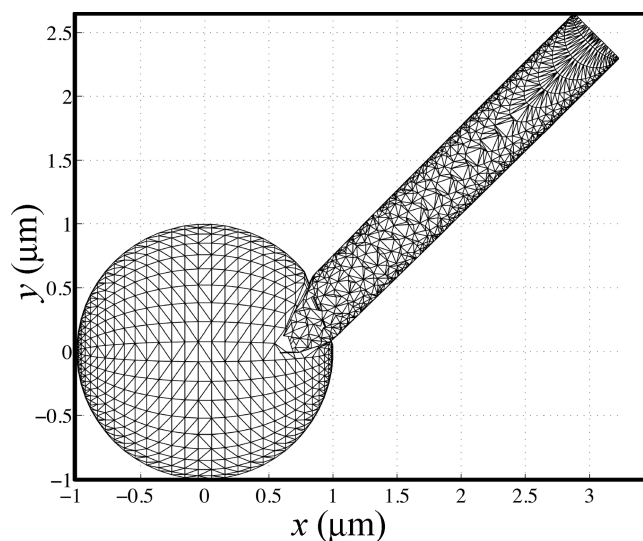


Figure 4. Typical nanomotor geometry used in the simulations corresponding to an arm length of $3.5 \mu\text{m}$ (axes labels are in micrometers). A nanomotor is modeled as a sphere connected to a section of an ellipsoid representing the arm. Sections of different lengths are removed from the free end of the ellipsoid to match experimental conditions. The figure also shows the mesh used in the regularized Stokeslet algorithm, which was obtained by parametrization of the sphere and ellipsoid surfaces.

After fabrication, each substrate was placed into a small glass vial with DI water, and the vial was then sonicated for <1 min to remove the nanomotors from the substrate and to suspend them in the water. Samples of $2 \mu\text{L}$ nanomotor suspension were dropped by pipet onto clean silicon slides for observation. Two microliter droplets of hydrogen peroxide of various concentrations were added to the nanomotor suspensions to activate the motion. The nanomotors were tracked using a charge-coupled device (Imperx IPX-VGA210) with a temporal resolution of 20 frames per second coupled with reflected light microscopy (Mitotoya FS-110) and custom-developed tracking software. Once the droplet is placed on the silicon wafer, the nanomotors quickly settle to the surface of the silicon substrate; we observe the swimming at the substrate surface so that they remain in the focal plane. The video files were analyzed using the tracking software to determine various parameters of interest such as speed, curvature, etc.

During observation, the optical microscope is focused on the observation slide, and since most of the particles settle to the surface, the particles move on the plane of the surface and the trajectories were observed in 2D. Because of the geometry of the structures shown in Figure 1a, the trajectories should be either linear or curved with perturbations arising from thermal fluctuations. To analyze the effect of changing the geometry of the particles, the extent to which the trajectories are altered needs to be determined. A natural value to calculate in order to characterize the trajectory of the curves is the curvature κ , which gives a quantitative value for how much the trajectory is changing direction with time. Our experiments return a list of the x and y coordinates of the particle, which describes motion over a certain time interval in accordance to translational and angular velocities \mathbf{v} and ω . The following method is used to determine the mean radius of curvature of the trajectories: the trajectories are divided into nearly circular sections that are fit with a circular path of equation $(x - a)^2 + (y - b)^2 = r^2$ whose radius r gives an estimate of the average radius of curvature of the section.

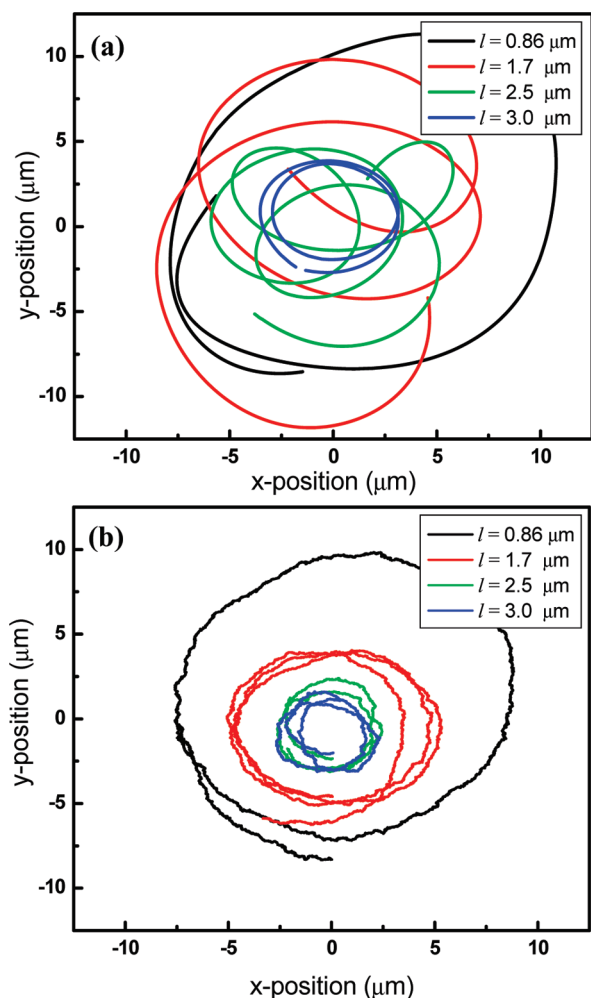


Figure 5. (a) The plot shows the trajectories of nanomotors with four different arm lengths $l = 0.86 \mu\text{m}$, $1.7 \mu\text{m}$, $2.5 \mu\text{m}$, and $3.0 \mu\text{m}$. As the arm length increases, the radius of curvature decreases until some unknown minimum is reached. Each plot is a 10 s interval, and the centers of each trajectory have been deliberately moved to a mutual middle. (b) Simulated nanomotor trajectories for the same arm lengths as in (a) showing similar trends as the experimental data. Axes labels are in micrometers. Also see accompanying online movie in Supporting Information.

Following Kása,⁴³ this is achieved by minimizing the sum of the squares of the distances from the discrete points (x_1, y_1) , (x_2, y_2) , ..., (x_n, y_n) on the trajectory section to points on the circle. Specifically, the following function is minimized over the unknown parameters a , b , and r

$$\text{SSK}(a, b, r) = \sum_{i=1}^n [r^2 - (x_i - a)^2 - (y_i - b)^2]^2 \quad (4)$$

Kása further points out that solutions for a and b can be obtained by solving linear equations, and the radius of curvature is then obtained as

$$r = \sqrt{\frac{1}{n} \sum_{i=1}^n [(x_i - a)^2 + (y_i - b)^2]} \quad (5)$$

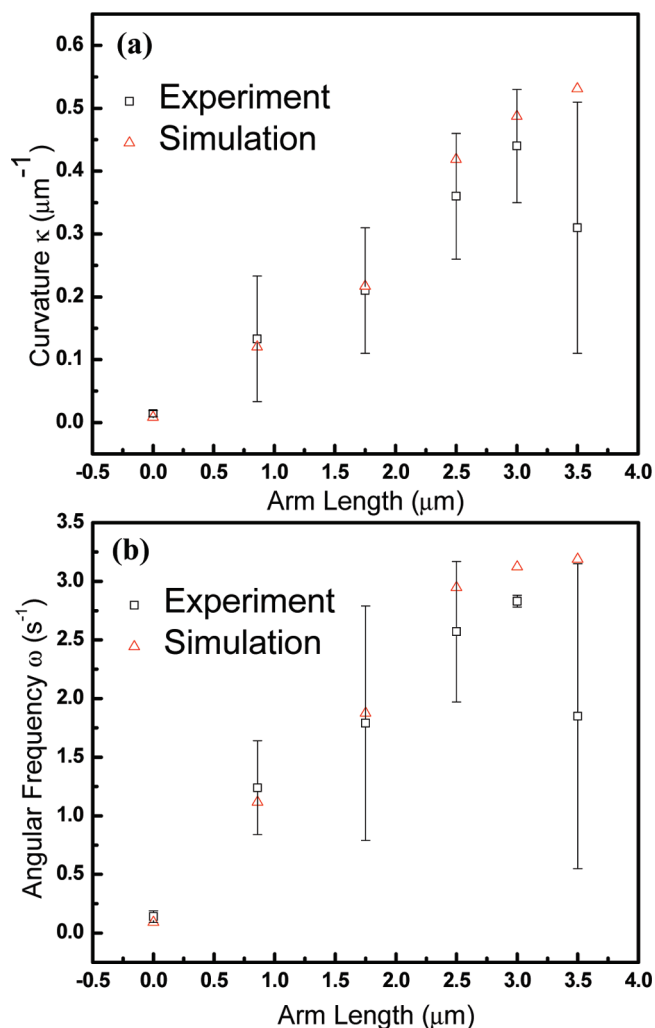


Figure 6. (a) Experimental (black \square) versus numerical values (red \triangle) for curvature κ versus TiO_2 arm length. For κ , both the numerical values and the experimental values follow the same trend of a roughly linear increase with the exception of the $l = 3.5 \mu\text{m}$ arm length; (b) experimental (black \square) versus numerical values (red \triangle) for angular frequency ω versus TiO_2 arm length. The simulation results show a similar relationship with experimental ω and appear to be reaching a limiting value as the arm length increases. The outlier as in Figure 5a appears to be $l = 3.5 \mu\text{m}$.

and averaged over all the trajectory sections. Finally, the mean trajectory curvature κ is determined as the inverse of the averaged radius of curvature obtained above.

The OAD-grown structures swim according to the translational and angular velocities resulting from the catalytic propulsion force via the mobility matrix (inverse of the resistance matrix of eq 1), which is a function of the nanomotor geometry and specifically of its arm length. Each nanomotor shown in Figure 2 exhibits a similar yet different swimming pattern when placed in the same concentration of H_2O_2 (10%) due to the various drag forces and torques applied to the arm corresponding to each length. Figure 5a,b shows two-dimensional (2D) plots showing representative experimental and numerical trajectories for nanomotors with various arm lengths, respectively. The samples shown are typical for each arm length. To clearly compare the different trajectories, each was adjusted to have a mutual center at

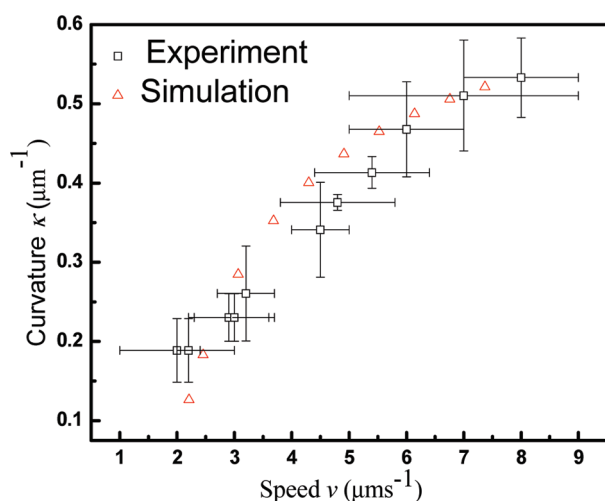


Figure 7. Experimental (black \square) versus numerical (red Δ) data for speed versus curvature κ . For the experiment, there exists a roughly linear increase of curvature with respect to speed (the speed is increased by increasing the concentration of H_2O_2). For the simulation results, a similar trend is seen for low speeds, but the curve flattens at higher speeds as opposed to staying linear.

the origin of the graph ($0 \mu\text{m}$, $0 \mu\text{m}$). All trajectories show roughly circular motion. The structure with the shortest arm ($l = 0.86 \mu\text{m}$, Figure 2b) moves with a relatively large radius in comparison to the other lengths; as the length of the arm increases, the radii of curvature become smaller. The nanomotors swim in a roughly circular pattern when the oxide arm is present. For each rotation with radius of curvature r , the structure spins once as it moves about the circular trajectory so that the angular velocity ω of the nanomotor also corresponds to the angular frequency of the circular motion. Figure 6a,b compares the experimental values (black \square) against the numerical values (red Δ) for arm length versus curvature κ and arm length versus angular frequency ω respectively, showing similar trends. Figure 7 compares experimental values (black \square) against numerical values (red Δ) for the effect of nanomotor speed on curvature κ in the $l = 3.5 \mu\text{m}$ case. The speed is altered by changing the concentration of H_2O_2 . Discussion of the comparison of experiment and simulation is presented below.

Figure 5a shows experimental results for swimming trajectories corresponding to four different arm lengths (excluding $l = 0 \mu\text{m}$ and $l = 3.5 \mu\text{m}$ for clarity). The graph in Figure 5b shows the corresponding simulation results (also see accompanying online movies in Supporting Information). It should be noted for the experiments that roughly constant velocity is observed for each arm length, and that each system is observed at steady state at which the applied force and torque are exactly countered by the forces and torques resulting from hydrodynamic drag and frictional forces with the substrate. In the absence of any Brownian fluctuations, the simulated trajectories are found to be closed circles with constant curvature, whose radius decreases with increasing arm length. With Brownian motion, the trajectories deviate from perfect circles but instead take the form of irregular orbits that are qualitatively similar to those observed in the experiments. The increase in the mean trajectory curvature with arm length is also consistent with the experimental observations. This is shown more quantitatively in Figure 6, where experimental values (black \square) are compared with values from

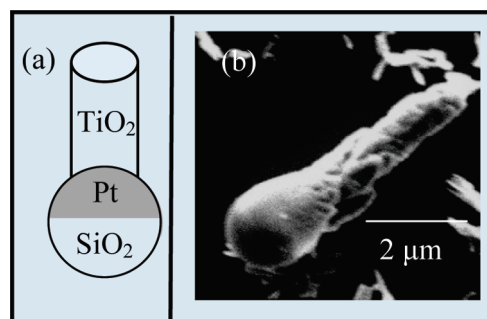


Figure 8. (a) Schematic of a GLAD-grown structure; (b) SEM.

simulations (red Δ) for κ (Figure 6a) and ω (Figure 6b). For the experimental results in Figure 6a, as the arm length increases, κ slightly increases in a roughly linear fashion except for the $l = 3.5 \mu\text{m}$ case, which does not follow this trend; the simulation data also follow a roughly linear increase with respect to l . In Figure 6b, ω follows a similar increase as κ with the $l = 3.5 \mu\text{m}$ case once again not following the same trend as the rest of the data points; the simulation data first increase linearly, but then begin to level as l increases. The large error bar for both the curvature κ and angular frequency ω may account for the outliers. It is expected that κ and ω will both reach a limiting value since increasing the arm length will eventually decrease the two values along with the velocity, that is, at a certain length, the driving force will only rotate the structure and no translational motion will be present (no circular trajectory, only rotation): as $l \rightarrow \infty$, $v \rightarrow 0$. The two graphs show similar trends and values, but the simulations seem to suggest that ω and κ will reach a limiting value for $l > 3.5 \mu\text{m}$, while this is unclear in the experimental data. Similar trends are observed for the curvature versus speed for experimental (black \square) versus simulation (red Δ) results as shown in Figure 7, where we find that good agreement is obtained at lower speeds, while the behavior at high speeds is not captured as accurately by the simulations. The experimental data points follow a linear increase, while the numerical values appear to be reaching a limiting value as the speed increases.

As a control experiment, we alter the position of the oxide arm on the microbead and observe the swimming trajectories. We have shown in a previous study with Pt-coated microbeads that increasing the concentration of H_2O_2 increases the speed of the microbeads and that their trajectories are linear due to symmetry.²¹ For the GLAD structures described in the fabrication section, a schematic and an SEM are shown in Figure 8a,b respectively. When the speed is modulated with the addition of various concentrations of H_2O_2 , increasing the speed should have little effect on the trajectories of the GLAD-grown structures since symmetry is still present; this is in opposition to the OAD-grown structures' trajectories, which have greater average curvature with increasing speed. The OAD-grown structures are expected to have greater torque since the drag increases concurrently with velocity. We subject the OAD-grown and the GLAD-grown structures to the same concentrations of H_2O_2 to see whether curvature is altered for the two. OAD-grown speed plots are shown in Figure 7; as we increase the speed of the OAD nanomotor, the curvature increases monotonically, which is expected while Figure 9 shows that the curvature remains roughly constant as the speed is increased in the case of a symmetric structure. The best-fit line for Figure 7a gives a slope of $6.4 \times 10^{-2} \text{ s}/\mu\text{m}^2$ while the slope for the GLAD

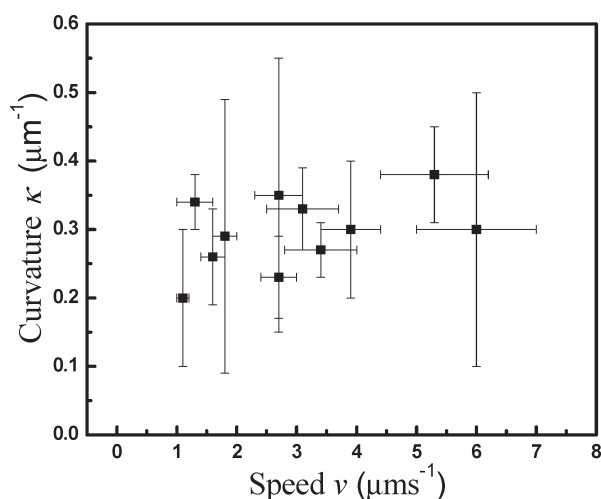


Figure 9. Speed versus curvature for the GLAD-grown structure showing roughly constant curvature for all speeds.

structure motion in Figure 9 is $1.5 \times 10^{-2} \text{ s}/\mu\text{m}^2$. The speed should have no effect on the GLAD structure as the arm is symmetric and should not result in a hydrodynamic torque, and Figure 9 suggests this is indeed occurring. Intuitively, a swimmer that is symmetric and is being propelled along its axis of symmetry should not feel any torque; the GLAD structure swims in an approximate straight line as expected (with fluctuations resulting from Brownian motion). This result strengthens the idea that the geometry of catalytic nanomotors has a major impact on swimming behavior and that modulation of behavior is possible through systematic design.

Using a dynamic fabrication method based on OAD and GLAD, we have studied the effects of geometry on the dynamics of catalytic nanomotors moving at low Reynolds number. The trajectories of the particles are highly dependent upon the geometry, and OAD/GLAD allows easy modulation of nanomotor morphology. The special case on which we focus is a nanomotor consisting of a spherical microbead head and an oxide arm that is off-centered to the driving force arising from the chemical reaction. We altered the length and angle of the oxide arm and compared the experimental results to a computational model based on a solution of the Stokes equations using the method of regularized Stokeslets. The two sets of results were found to be very similar with small discrepancies that may be attributed to the idealized configuration adopted in the simulations in which the nanomotor arm was assumed to remain parallel to the supporting substrate. As the field of catalytic nanomotors matures, our study demonstrates that scientists and engineers should consider the influence of nanomotor shape and geometry upon swimming behavior in order to design better structures in the future.

■ ASSOCIATED CONTENT

S Supporting Information. (1) A movie showing swimming nanomotor with a silica microbead head and a titania arm. (2) Movie showing swimming patterns obtained from simulations; as the length of the arm decreases, the radius of curvature increases. This material is available free of charge via the Internet at <http://pubs.acs.org>.

■ AUTHOR INFORMATION

Corresponding Author

*E-mail: jggibbs@physast.uga.edu.

■ ACKNOWLEDGMENT

We acknowledge the financial support from the National Science Foundation under Contract No. CMMI-0726770 (J.G. and Y.Z.) and from a fellowship from FMC Technologies Inc. (S.K.). We also thank Christopher Hoffman for his design of the tracking software.

■ REFERENCES

- (1) Mavroidis, C.; Dubey, A.; Yarmush, M. L. *Annu. Rev. Biomed. Eng.* **2004**, *6*, 363–395.
- (2) Wang, J.; Manesh, K. M. *Small* **2010**, *6* (3), 338–345.
- (3) Mirkovic, T.; Zacharia, N. S.; Scholes, G. D.; Ozin, G. A. *Small* **2010**, *6* (2), 159–167.
- (4) Ozin, G. A.; Manners, I.; Fournier-Bidoz, S.; Arsenault, A. *Adv. Mater.* **2005**, *17* (24), 3011–3018.
- (5) Paxton, W. F.; Sundararajan, S.; Mallouk, T. E.; Sen, A. *Angew. Chem., Int. Ed.* **2006**, *45* (33), 5420–5429.
- (6) Browne, W. R.; Feringa, B. L. *Nat. Nanotechnol.* **2006**, *1* (1), 25–35.
- (7) Hong, Y. Y.; Velegol, D.; Chaturvedi, N.; Sen, A. *Phys. Chem. Chem. Phys.* **2010**, *12* (7), 1423–1435.
- (8) Soong, R. K.; Bachand, G. D.; Neves, H. P.; Olkhovets, A. G.; Craighead, H. G.; Montemagno, C. D. *Science* **2000**, *290* (5496), 1555–1558.
- (9) Ismagilov, R. F.; Schwartz, A.; Bowden, N.; Whitesides, G. M. *Angew. Chem., Int. Ed.* **2002**, *41* (4), 652–+.
- (10) Catchmark, J. M.; Subramanian, S.; Sen, A. *Small* **2005**, *1* (2), 202–206.
- (11) Fournier-Bidoz, S.; Arsenault, A. C.; Manners, I.; Ozin, G. A. *Chem. Commun.* **2005**, *4*, 441–443.
- (12) Vicario, J.; Eelkema, R.; Browne, W. R.; Meetsma, A.; La Crois, R. M.; Feringa, B. L. *Chem. Commun.* **2005**, *31*, 3936–3938.
- (13) Qin, L. D.; Banholzer, M. J.; Xu, X. Y.; Huang, L.; Mirkin, C. A. *J. Am. Chem. Soc.* **2007**, *129* (48), 14870–+.
- (14) He, Y. P.; Wu, J. S.; Zhao, Y. P. *Nano Lett.* **2007**, *7* (5), 1369–1375.
- (15) Ghosh, A.; Fischer, P. *Nano Lett.* **2009**, *9* (6), 2243–2245.
- (16) Solovev, A. A.; Mei, Y. F.; Urena, E. B.; Huang, G. S.; Schmidt, O. G. *Small* **2009**, *5* (14), 1688–1692.
- (17) Gibbs, J. G.; Zhao, Y. P. *Small* **2009**, *5* (20), 2304–2308.
- (18) Paxton, W. F.; Kistler, K. C.; Olmeda, C. C.; Sen, A.; St; Angelo, S. K.; Cao, Y. Y.; Mallouk, T. E.; Lammert, P. E.; Crespi, V. H. *J. Am. Chem. Soc.* **2004**, *126* (41), 13424–13431.
- (19) Dhar, P.; Fischer, T. M.; Wang, Y.; Mallouk, T. E.; Paxton, W. F.; Sen, A. *Nano Lett.* **2006**, *6*, 66–72.
- (20) Laocharoensuk, R.; Burdick, J.; Wang, J. *ACS Nano* **2008**, *2* (5), 1069–1075.
- (21) Gibbs, J. G.; Zhao, Y. P. *Appl. Phys. Lett.* **2009**, *94*, 163104.
- (22) Demirok, U. K.; Laocharoensuk, R.; Manesh, K. M.; Wang, J. *Angew. Chem., Int. Ed.* **2008**, *47* (48), 9349–9351.
- (23) Howse, J. R.; Jones, R. A. L.; Ryan, A. J.; Gough, T.; Vafabakhsh, R.; Golestanian, R. *Phys. Rev. Lett.* **2007**, *99*, 048102.
- (24) Ibele, M.; Mallouk, T. E.; Sen, A. *Angew. Chem., Int. Ed.* **2009**, *48* (18), 3308–3312.
- (25) Gibbs, J. G.; Zhao, Y. P. *Small* **2010**, *6* (15), 1656–1662.
- (26) Sundararajan, S.; Lammert, P. E.; Zudans, A. W.; Crespi, V. H.; Sen, A. *Nano Lett.* **2008**, *8* (5), 1271–1276.
- (27) Wang, Y.; Hernandez, R. M.; Bartlett, D. J.; Bingham, J. M.; Kline, T. R.; Sen, A.; Mallouk, T. E. *Langmuir* **2006**, *22* (25), 10451–10456.

- (28) Kovtyukhova, N. I. *J. Phys. Chem. C* **2008**, *112* (15), 6049–6056.
- (29) Kline, T. R.; Paxton, W. F.; Mallouk, T. E.; Sen, A. *Angew. Chem., Int. Ed.* **2005**, *44* (5), 744–746.
- (30) Calvo-Marzal, P.; Sattayasamitsathit, S.; Balasubramanian, S.; Windmiller, J. R.; Dao, C.; Wang, J. *Chem. Commun.* **2010**, *46* (10), 1623–1624.
- (31) Gangwal, S.; Cayre, O. J.; Bazant, M. Z.; Velez, O. D. *Phys. Rev. Lett.* **2008**, *100*, 058302.
- (32) Balasubramanian, S.; Kagan, D.; Manesh, K. M.; Calvo-Marzal, P.; Flechsig, G. U.; Wang, J. *Small* **2009**, *5* (13), 1569–1574.
- (33) Happel, J.; Brenner, H. *Low Reynolds number hydrodynamics, with special applications to particulate media*; Kluwer: Norwell, MA, 1983.
- (34) Kim, S.; Karrila, S. J. *Microhydrodynamics: Principles and Selected Applications*; Dover: Mineola, NY, 1991.
- (35) Cortez, R. *Siam J. Sci. Comput.* **2001**, *23* (4), 1204.
- (36) Pozrikidis, C. *Boundary integral and singularity methods for linearized viscous flow*; Cambridge University Press: Cambridge, U.K., 1992.
- (37) Ainley, J.; Durkin, S.; Embid, R.; Boindala, P.; Cortez, R. *J. Comput. Phys.* **2008**, *227* (9), 4600–4616.
- (38) Smith, D. J. *Proc. R. Soc. London, Ser. A* **2009**, *465* (2112), 3605–3626.
- (39) Blake, J. R. *Proc. Cambridge Philos. Soc.* **1971**, *70*, 303–310.
- (40) Bhushan, B. *Springer Handbook of Nanotechnology*, 2nd ed.; Springer: Heidelberg, Germany, 2007.
- (41) Liu, H. W.; Bhushan, B. *Ultramicroscopy* **2003**, *97* (1–4), 321–340.
- (42) Russel, W. B. *Annu. Rev. Fluid Mech.* **1981**, *13*, 425–456.
- (43) Kása, I. *IEEE Trans. Instrum. Meas.* **1976**, *25*, 8–14.